Low Efficiency of Laser Heating of Gold Particles at the Plasmon Resonance: An X-ray Calorimetry Study

Anton Plech,* Anna R. Ziefuß, Matteo Levantino, René Streubel, Stefan Reich, and Sven Reichenberger*

ABSTRACT: Laser excitation of nanoparticles provides an appealing tool for particle engineering as well as nanoscale-localized photothermal material modification. In the case of plasmonic nanoparticles like gold, mostly on-resonant excitation is used as it appears to be the most efficient channel for laser heating. Yet, as will be shown in this paper, in the case of an excitation with picosecond pulse duration a drastic reduction of the energy uptake efficiency of gold nanoparticles is observed at on-resonant excitation with 532 nm compared to interband excitation at 400 nm. This observation is found irrespective of varied gold nanoparticle size or different synthesis methods. Based on the nanocalorimetry of laser-excited suspended gold nanoparticles with time-resolved X-ray scattering the transient particle temperature, heat-induced relaxation and particle expansion and nonreversible particle transformations were disentangled. At first glance, the lower heating efficiency appears related to ultrafast plasmon bleaching and its recovery in the picosecond range. Yet, following a caloric heat balance a significant residual dissipation channel remains in the case of on-resonant excitation, which is absent at interband excitation. Consequently, photothermal applications may suffer from lower heat generation at the expense of irreversible channels.

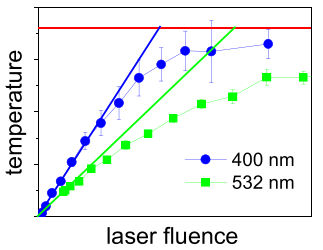

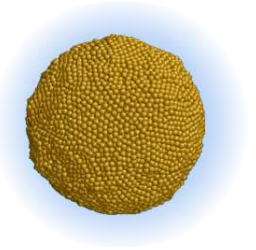

KEYWORDS: *plasmon resonance, gold nanoparticles, picosecond laser, nanoparticle heating, bleaching*

Plasmonic nanoparticles, as of gold or silver, represent an appealing tool for nanoscale-localized transduction of (pulsed) laser light into electron injection, heat generation, or structural modifications on the nanoscale. The large absorption cross section, absent blinking[1] and options to tailor the resonance through particle shapes and composition, allow for ubiquitous applications, such as hyperthermia,[2−4] membrane poration,[5,6] near-field pattering,[7−9] or diagnostic applications,[10,11] just to name a few. Numerous publications reveal the underlying mechanisms, which are now understood to a high level of detail. Photoexcitation with visible/near-IR light elevates bound or conduction-band electrons into free states, whereupon thermalization of the electron gas and interaction with the phonon bath converts the deposited energy into heat. Depending on sizes and relaxation times, the thermal energy of the lattice is released into the environment or taken up into latent heat of phase transformations, such as melting or evaporation.[12] The strongly localized heat can modify the environment on a nanometer scale by producing vapor bubbles in suspension or emitting photoacoustic pulses,[13,14] which add shear forces to structures close to the excited nanoparticles. The time scales, upon which these steps enroll, range from a few-femtosecond plasmon dephasing and picoseconds of electron thermalization and electron−phonon coupling to hundreds of picoseconds for heat transduction and structural transformations.

Yet, in practice, experimental photoexcitation studies have reported vastly different efficiencies for heat deposition[15−17] and related thermal threshold processes, such as particle melting or bubble formation.[18] We have recently noticed that the transient lattice expansion, representing particle heating after picosecond laser excitation of gold nanospheres,[17] or nanorods[16] was found to be less than predicted by optical calculations, if the plasmon-resonant wavelength of 532 nm, respectively 800 nm (for rods), is used. This may be complicated by morphology effects in particles of different synthesis origins.[19,20]

The general notion is that gold nanoparticle excitation close to the surface plasmon resonance (SPR), which can be reached at 532 nm for gold spheres of sizes between 5 and 100 nm is favorable for most efficient excitation and for utilizing near-field effects to obtain localized excitation on the nanoscale.[21] Yet, lower efficiency at the SPR as compared to shorter wavelengths at the interband transition of gold have been described.[22,23] Wavelength-dependent bacteria inactivation was studied by Tatsuno et al.[4] with nanosecond laser pulses and found to be

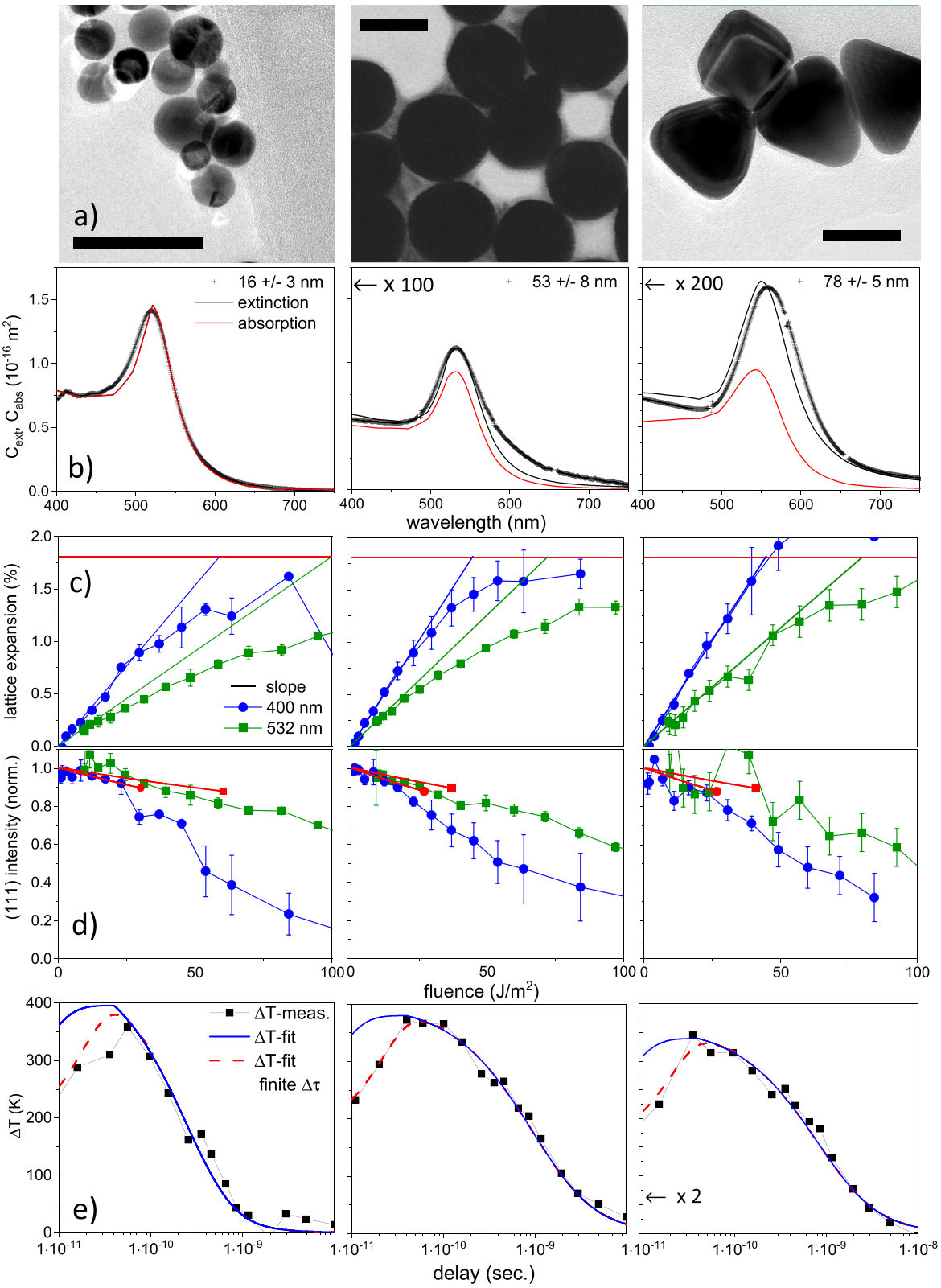

Figure 1. Sample characterization and time-resolved calorimetry of selected batches: citrate particles of 16 ± 3 nm (root-mean-square deviation) diameter (left), PLAL particles of 53 ± 10 nm (center) and CTAB particles of 78 ± 5 nm particles (right). The rows display from top to bottom: (a) TEM micrographs (scale bars each 50 nm); (b) measured UV−vis extinction in arbitrary units scaled to the calculated absorption and extinction cross section.[29] The crosses in part b are measured, lines are calculations, the absolute cross sections for 53 and 78 nm particles have been scaled by 100 and 200, respectively, relative to that of 16 nm particles. Furthermore: (c) relative lattice expansion at 55 ps as a function of laser fluence at 400 nm (blue) and 532 nm (green) together with lines for initial slopes (blue and green) and Δ_{max} (red); (d) relative intensity change of the (111) reflection at 55 ps together with the bulk Debye−Waller factor (red line) at a temperature conforming to the observed lattice expansion; and finally, (e) the time-resolved lattice expansion converted into temperature (symbols) together with a fit (line) of the cooling kinetics (see text).

more efficient at 420 nm as compared to wavelengths closer to the SPR. They stress the importance of scattering on the biological action. Also in laser fragmentation a more efficient interband heating was discussed by Hashimoto et al.[8]

This raises the question, whether fundamental steps in energy conversion depend on the spectral excitation region. Minutella et al. studied ultrafast electron dynamics of gold particles and found longer electron−phonon coupling times at the interband transition related to higher heating efficiency, but otherwise no size- or wavelength-dependence close to the SPR.[24] Staechelin et al. demonstrated strong dependence of the coupling time on particle crystallinity[25] that points toward real-structure effects acting on an observed efficiency of excitation. Although all these general indications for a more efficient interband heating exist, no systematic verification has been conducted up until now, where the phase transition and crystal structure evolution of the colloidal gold nanoparticles are being studied with ultrashort time resolution at on- and off-resonant laser excitation.

The present study intends to provide this missing verification by comparing the laser excitation and structure response of gold colloids of varied size and morphologies at either the plasmon resonance or the interband absorption by a time-resolved laser-pump, X-ray-probe study. Pulsed X-ray scattering with 60 ps resolution records the absolute amount of gold nanoparticle heating at the SPR or interband transition for a set of differing particle morphologies, laser-ablated ligand-free gold particles in liquid (PLAL),[26] chemically synthesized, polycrystalline particles by citrate,[27] and highly crystalline particles by a seeded process (CTAB).[28]

RESULTS

Figure 1 compiles selected data for the different particle morphologies (citrate, PLAL and CTAB) and selected particle sizes. The TEM data (Figure 1a) and Supporting Information) show an ensemble of spherical particles with visible size dispersion for the citrate particles and shape dispersion for the large CTAB particles. Smaller CTAB particles (shown in the Supporting Information) display high sphericity.

The size distribution of the PLAL particles peaks at 53 nm, but a smaller population of particles <20 nm is present, which origins from the ablation mechanism[30,31] (see Figure S2 of the Supporting Information). Nevertheless, the extinction curves match very well with the Mie calculations (Figure 1b, performed with comparable average particle size found from TEM, respectively SAXS), except for a weak red-shifted pedestal for the PLAL particles and a systematic red shift of the plasmon peak for the CTAB particles due to the organic shell, which is not included in the Mie calculations.

The transient heating of the gold particles is deduced from the time-resolved powder scattering by the shift of the Bragg angle of the (111) reflection to lower angles and also manifested by a reduction of reflection intensity due to thermal disorder (see Figure 1, parts c and d). Under the assumption that this peak shift is proportional to the lattice expansion $\Delta a/a$ and thus particle heating ($\Delta T/T$), a transient temperature can be assigned to the particles as a function of laser fluence and delay between the laser (pump) pulse and the X-ray (probe) pulses.[32] Limitations to this notion should be critically addressed. First, the lattice expansion and latent heat of the gold particles may deviate from the used bulk values. This could indeed be the case for very small particles approaching the quantum size limit. Large particles nevertheless have earlier been investigated to show bulk-like behavior in thermal expansion[33] and fluence-dependent lattice change.[34] While both thermal lattice expansion and latent heat are not precisely linear in temperature, the combined caloric effect on lattice expansion is only deviating by a few percent from linearity. Diroll et al.[35] discuss an anomalous heat capacity of a TiN suspension upon laser excitation. Such effects may appear in more complicated systems and/or if phase transitions are approached, which will be discussed below. Second, thermal equilibrium is assumed, when the shift is assigned to a temperature.[34] From the results in Figure 1e), a maximum heating is observed at a delay of 55 ps, which coincides with a maximum in lattice expansion.

The observed delay for this maximum is caused by the convolution of finite lattice expansion and the time resolution of the experiment. The inclusion of the resolution effect is discussed below. At this delay, we expect efficient phonon thermalization, such that the lattice expansion can be interpreted as particle heating. A deviation from this thermalization can occur for size-related vibrations[36−38] of the largest particles. Particles of 150 nm diameter possess a vibrational mode of 50 ps,[38] which will modulate the scattering profile[39] and can lead to an overshoot in expansion relative to the thermal equilibrium. Still, the vibration carries only a small fraction of the total energy. Last, plastic or irreversible lattice deformation cannot be excluded *a priori*, such as weak particle erosion[40] or beginning of melting, including surface melting. Such irreversible effects will also emanate in the loss of crystallinity and thus reduction of the (111) peak intensity at higher fluence, when approaching the melting transition.

The change of lattice parameter for the selected samples is shown in Figure 1c), suggesting a linear slope versus applied laser fluence at the shortest possible positive delay. Nevertheless, this linearity is violated for larger fluence to end with a vanishing slope. This behavior shows that an inelastic modification takes place, as the peak intensity is seen to decay at the same time. Indeed, the horizontal line marks the maximum lattice expansion Δ_{max} that bulk gold would sustain before melting in thermal equilibrium. The expansion slope reduces, when approaching this boundary, confirming particle melting at a delay of 55 ps and high fluence. The peak intensity vanishes over a finite range in fluence (part d of Figure 1). This range is on the one hand given by the latent heat during melting, which limits lattice expansion while dissipated heat is transformed into melting solid gold. Takami et al.[41] proposed a simple model, where sustained energy increase of excited nanoparticles would lead to a strictly linear particle heating before reaching a plateau in lattice temperature in the two-phase region between solid parts and liquid parts of the particle. This assumes a consecutive transformation of energy into heat and later melting at the melting point. On an ultrafast time scale, however, melting may occur in parallel to lattice expansion, such that increasing lattice expansion and peak intensity drop evolve in parallel. On the other hand, the unavoidable distribution in energy density across the nanoparticle ensemble (both due to spatial and temporal laser fluctuations and the particle size distribution) leads to a further smearing of the slope. This explains the observation of a slope reduction: at sufficiently high fluence the first fraction of particles starts to melt, while the less excited fraction is still crystalline and shows a reduced expansion, scaling with its lower temperature.

We concentrate on the (initial) slope of lattice expansion versus laser fluence. This is a quantity that can be calculated when using the particle absorption cross section and the thermal parameters of gold, such as thermal lattice expansion and heat

capacity.[34] Linear functions are added to Figure 1c) to indicate the extracted slope. The first observation already meets the eye: the slope at an excitation wavelength of 532 nm is smaller than that at 400 nm. This is not expected, as the absorption cross section of the Mie calculation predicts the opposite. The peak intensity in each case first follows the measured slope, but shows a stronger decay when the expansion exceeds 1% and approaches the maximum expansion of bulk gold at the melting point. The intersection of both lines may be assigned as the critical fluence for the start of the melting process. The melting transition is more directly visualized, when the peak intensity is plotted as a function of the observed lattice expansion, which serves as an internal thermometer. Figure 2 shows this relation

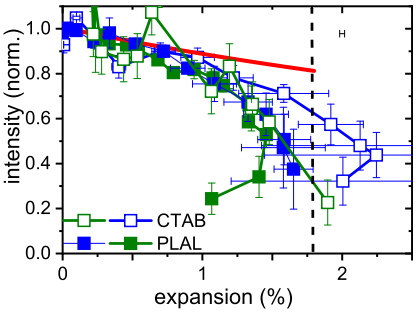

Figure 2. Relative intensity change of the (111) reflection of 53 nm PLAL particles (full symbols) and 78 nm CTAB particles (open symbols) as a function of the relative lattice expansion at 55 ps together with the bulk Debye–Waller factor at a temperature conforming to the lattice expansion (red line) at 532 nm excitation (green symbols) and 400 nm (blue symbols). The dashed vertical line marks the maximum lattice expansion at the melting point of bulk gold.

for PLAL and CTAB particles together with a calculation of the Debye–Waller factor of the corresponding temperature. The initial intensity decay below an expansion of 1% closely follows the predicted behavior, indicating a pure elastic thermal excitation. Above that value a stronger decay is observed leading to a complete loss of crystallinity at about 1.68%, very close to the bulk limit of 1.78%.[42] Note that both 400 and 532 nm excitation follow a similar behavior, which is seen in the other samples as well (see Supporting Information). We therefore conclude that lattice thermalization proceeds in a qualitatively similar way in both cases. However, when comparing the laser-generated 53 nm and the chemically prepared 78 nm CTAB-covered gold nanoparticles in Figure 2, the chemically prepared particles show a slightly different behavior. The lattice expansion even overshoots the expected melting point expansion, at least for a fraction of the still crystalline particles. This may be related to a higher yield strength of single-crystalline particles with less lattice defects and thus an elastic overshoot before melting.

The temporal evolution of the lattice expansion is shown in Figure 1e) together with simulations of heat transfer into the water medium. Fluences corresponding to a lattice expansion of 0.6–1% were chosen in order not to reach the melting region. Typical cooling times range from 200 ps for the smallest to 1 ns for the largest particles. The shortest decay times for the smallest particles are already close to the temporal resolution; therefore, the effect of this convolution has to be taken into account. The dashed lines in Figure 1e) represent the temporal temperature change convoluted with the X-ray time resolution. In particular, for the smallest particles, the observed heating is less than the uncorrected simulated one. A modification of cooling originating from a slow electron–phonon coupling in gold,[43−45] which would modify temperature rise and therefore dissipation via cooling during electron–phonon coupling, has been neglected at this point as the effect would be small. The resolution effect is taken into account when determining an effective slope of temperature (lattice expansion) versus applied fluence.

The calculated slope from the theoretical absorption cross section both with and without temporal resolution effect is shown in Figure 3 together with the measured slopes for the

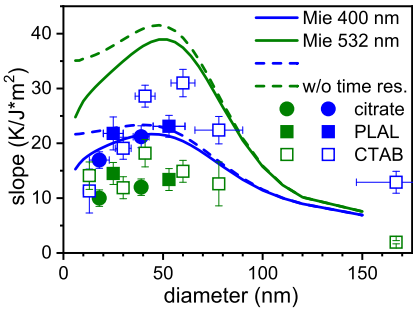

Figure 3. Measured expansion slope as a function of particle diameter for laser excitation at 400 nm (blue symbols) and 532 nm (green symbols). The lines represent the calculated expansion slope for Mie theory. The dashed lines are the direct calculations for 400 and 532 nm for 100% efficiency of conversion into heat and detection, while the full lines include a reduction of observed expansion with the 60 ps time resolution and onset of heat dissipation on this time scale.

investigated samples. The ratio between the measured slopes and the calculated one can be interpreted as an efficiency for heat conversion. Laser excitation at 400 nm indeed yields measured values close or even above the calculation, while at 532 nm a strong reduction of the efficiency by up to a factor of 3 is found. While the spread over the samples is considerable, we find no systematic differences depending on either of the synthesis procedures, except for a slightly higher efficiency for CTAB particles. The efficiency loss for 532 nm is consistent and thus not a direct consequence of a synthesis-related difference in particle morphology, crystallinity, or deviation from sphericity. In fact, the plasmon-resonant excitation of gold nanorods at 800 nm earlier showed a similar, if not higher loss in efficiency.[16]

DISCUSSION AND CONCLUSIONS

Regarding the efficiency results in Figure 3, it is evident that plasmon-resonant excitation of gold colloids to high lattice temperatures leads to a loss in efficiency as compared to interband excitation. This is, however, not completely unexpected and has been reported earlier.[22,23,46] Werner et al.[22] attribute this to the particular way that electron heat capacity is changed upon inter- versus intraband excitation. Furthermore, the bleaching effect at the plasmon resonance of gold colloids has been extensively studied in transient absorption spectroscopy.[24,43,45,47] Typical experiments excite the suspension at either 400 or 532 nm with femtosecond pulses and record the transient absorption change across the spectrum. The change of the plasmon resonance helped to discern the effects of plasmon dephasing, electron–electron thermalization, and electron cooling via electron–phonon coupling.[48] According to these steps, the absorption is described to bleach within a subpicosecond step and recover within a few picoseconds at the SPR, depending on the speed of electron–phonon coupling.

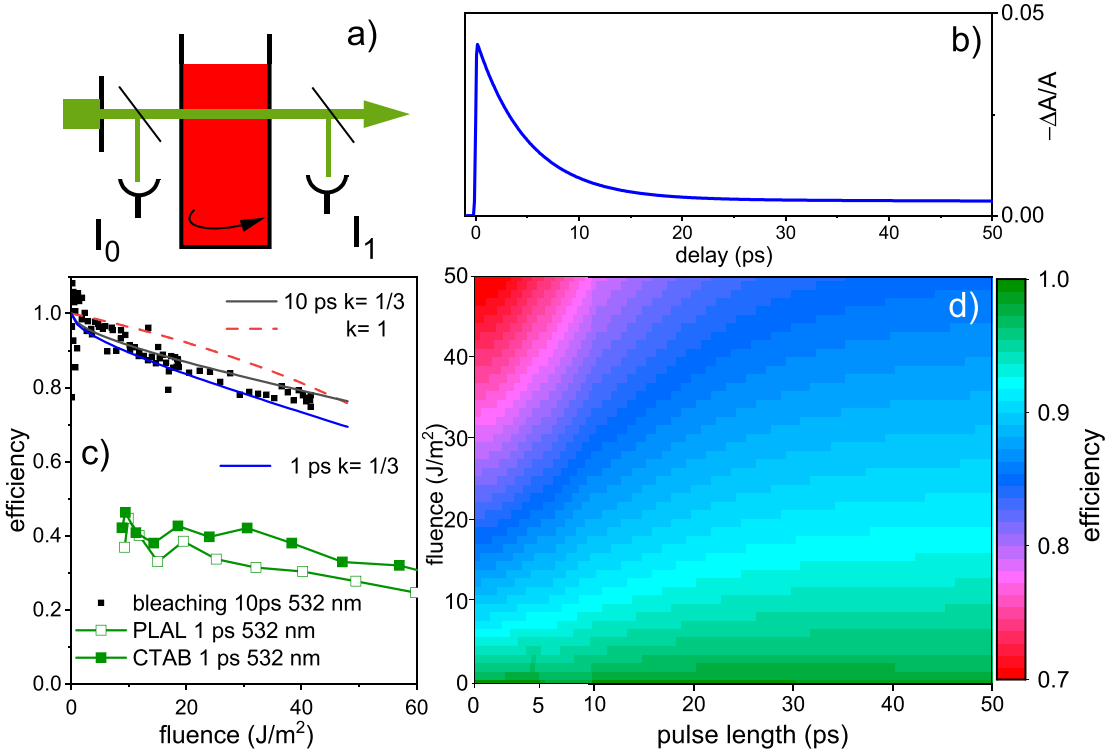

Figure 4. Prediction of the bleaching effect on the pulsed excitation at 532 nm for 53 nm PLAL particles: (a) bleaching is measured as the fluence-dependent change of transmitted laser intensity I_1 relative to the incoming intensity I_0 through a cuvette; (b) change of the absorbance as a function of time delay as proposed in eq 1; (c) bleaching as a function of laser fluence together with the predictions according to eq 1 for at $k = 1$ (dashed line) and $k = {}^1/_3$ (full lines) at 1 and 10 ps pulse length, respectively. The experimental efficiencies of heat generation in the nanoparticles are compared and taken from the fluence-dependent lattice expansion from Figure 1 divided by the expected slope from Mie theory (Figure 3): (d) false color plot of the expected reduction of efficiency through bleaching alone as a function of fluence and laser pulse length as discussed in the text ($k = {}^1/_3$).

The latter is dependent on the excitation density, as the electron heat capacity scales with electron temperature.[49] Typical recovery times of 4−6 ps are observed, but a dependence on the surface chemistry may shift the times.[50] A minor persistent bleach recovers within hundreds of picoseconds, reflecting the particle cooling via coupling to the environment. A second bleaching channel previously discussed in the literature occurs on a nanosecond time scale, when the particle heat transfer into the liquid leads to the formation of a vapor bubble, which changes the refractive index around the particle and leads to a damping of the plasmon resonance.[51,52] These bubbles show lifetimes of hundreds of picoseconds, up to nanoseconds.[34,53] The onset of this cause for bleaching is, however, related to bubble growth and thus delayed relative to the discussed pulse lengths of picoseconds and should matter only for longer pulses.

On the basis of these known temporal bleaching effects, a loss in absorption efficiency throughout on-resonant 532 nm excitation is to be expected, while simultaneously the absorption efficiency at interband absorption (400 nm) is only affected at bubble formation. Contrarily, at 400 nm a weak absorption increase is reported.[54] This could in a similar fashion explain the higher efficiency relative to the calculation in Figure 4.

We have estimated the bleaching effect by modeling the transient absorbance change (see Figure 4a−c) of the Mie cross section by

$$\Delta A(t)/A(-\infty) = -A_0 \cdot F^k \cdot (\mathrm{erf}(t/t_0) + 1) \times (\mathrm{e}^{(-t/t_1)} + A_1 \cdot \mathrm{e}^{(-t/t_2)}) \quad (1)$$

with erf being the error function for a rising signal with characteristic time t_0, and recovery of the bleaching by electron−phonon coupling (t_1) and particle cooling (t_2). The parameters A_0 and A_1 represent the amplitude of the bleaching and the relative contribution of the equilibrated electron−phonon bath, respectively. The amplitude A_0 scales with the excitation density and thus with the instantaneous fluence F. This scaling could be nonlinear, indicated by the exponent k. This function is convoluted with the temporal beam profile (assumed as Gaussian) in order to obtain the effective absorbed energy as a function of fluence and pulse length.

Figure 4d) shows a false-color map of the calculated efficiency as a function of laser pulse length and pulse fluence (right diagram) as well as selected fluence-dependent efficiency functions for $k = 1$ and $k = {}^1/_3$ (left diagram). The parameters used in eq 1 are $t_0 = 0.05$ ps, $t_1 = 5$ ps, and $t_2 = 500$ ps, reflecting the observed cooling times. The relative bleaching after electron−phonon thermalization A1 is chosen to be 0.1 to obtain a good fit. This is compared to the observed efficiency of heating of 53 nm PLAL particles and 78 nm CTAB particles at 1 ps pulse length and the measured transmission change (bleaching) through the suspension of 53 nm PLAL particles at 10 ps laser pulses, both at 532 nm, see Figure 4c.

If the amplitude $A_0 \times F$ is assumed to change linearly with fluence and temperature, respectively, then the calculated efficiency is starting at unity at low fluence to gradually (linearly) decay. Indeed, the bleaching of the PLAL suspension can be explained by this effect assuming a factor A_0 of 0.03. Yet, the experimental bleaching drops faster at lower fluence, which points toward a nonlinear bleaching, i.e., the bleach amplitude

does not grow linearly with fluence. The bleaching accounts for some 10−20% and is in good agreement with the prediction of the damping of the plasmon resonance and its recovery on the picosecond time scale. However, the observed heat in the particles is still less than bleaching included, as seen by low values around 0.3−0.5 for the range of fluences up to the inelastic modifications when approaching the melting point. Moreover, the observed efficiency loss already starts at low fluence and shows no asymptotic approach to 1 toward $F = 0$.

Therefore, it is implied that additional channels of energy dissipation exist that deviate the impact laser energy from the direct beam. There are several possible effects that could contribute to this:

(i) Scattering could be enhanced with an excited plasmon, which would affect 532 nm wavelength stronger than 400 nm. Earlier, effects of increased scattering have been discussed by several publications.[55−57] Hwang et al.[55] show that the scattering (respectively photoluminescence) follows the electron−phonon equilibration and is thus transiently enhanced. However, as the scattering cross section in Mie scattering is a rapidly varying function of particle size, this effect should not affect the smallest particles in the same way, as their scattering contribution vanishes relative to the absorption. Higher scattering losses are also expected, if adjacent particles couple through their plasmon resonance. This coupling can occur before particles actually touch. This coupling has been investigated by Magnozzi et al.[23] and led to a reduced efficiency at 532 nm. In that context, it is interesting to note that the CTAB particles are better stabilized such that plasmon coupling would have a lower effect. This could contribute to the slightly higher efficiency as seen in Figure 2.

(ii) The resonantly excited plasmon at 532 nm can cause different dissipation channels, such as photoelectron emission or microplasma formation.[58−60] In this case, energy is dissipated into the system but not detected as particle heating. Electron emission is a well established dissipation channel;[58,59] however, the discussed yield of several hundreds of electrons at moderate laser fluence would only carry a minor fraction of the absorbed energy of the particle.

(iii) Also, a direct coupling of the plasmon into exciting the adjacent water layer could divert energy from the particle directly into the aqueous shell around the particle. Zhao et al.[61] have recently studied theoretically and by molecular dynamics simulations the energy transfer across the particle−water interface upon laser irradiation. They argue about direct coupling into the water phase and enhancement of conduction. This could be accompanied by water splitting.[62,63]

(iv) Finally, inelastic processes of the particle lattice could contribute to a diversion of energy from the observed heating channel. At higher excitation beyond 1% in lattice expansion near-field ablation has been observed,[40] but also surface melting, or defect annealing, could contribute to energy uptake. A small indication might be that the relation between lattice expansion and Bragg peak intensity reduction shows slight differences between 400 and 532 nm excitation as indicated in Figure 2, in particular for the CTAB particles.

One should be aware that a discrepancy between the theoretical Mie spectra and the real particle absorption could be present. Indeed, a slight effect from nonideal spherical shape and internal morphology could broaden the plasmon resonance. This contribution is minor (see Figure 1), but it could cause a slight reduction in efficiency for the less perfect citrate and PLA particles in Figure 3. In ref 17, we also checked the efficiency of 53 nm PLAL particles for the macroscopic absorption cross section at known mass concentration and found a similar reduction. On the other hand, recent careful evaluation of experimental UV−vis spectra of model gold particles has confirmed the general reliability of the Mie calculations and size determination[64] at the interband transition, where our observed efficiency matches the prediction.

The observed reduction in efficiency of heat generation in picosecond-laser excited nanoparticles, therefore, is a sum of several effects. A quasi-linear effect sets in a low laser fluence and accounts for optical bleaching and enhanced scattering in concentrated suspension. Nonlinear fluence-dependent dissipation channels include plastic particle modification (including changing shape) and direct energy coupling into the near field (water medium). Therefore, a severe reduction in efficiency could possibly also be observed for high-intensity cw laser heating. As result, energy dissipation through resonant excitation at the plasmon resonance may be enhanced beyond the pure plasmon bleaching on a picosecond time scale by nonreversible effects. This could limit the reversibility of the photoexcitation process and the longevity of the particles in photothermal applications. An observed difference between PLAL and CTAB particles indicates a relation to real structure, such as yield strength or plasmonic particle coupling.

In conclusion, we have observed a consistent reduction of heat generation efficiency when gold colloids are excited at the plasmon resonance as compared to the interband transition. Pulsed X-ray scattering is used as a calorimeter to determine the transient particle temperature. It is thus a more direct tool than optical spectroscopy. On the other hand, it may miss ultrafast dissipation channels, which may be accounted for in quasistatic experiments recording the overall temperature rise. This reduction in efficiency can only partly be explained by a transient bleaching of the plasmon resonance. Beyond that further dissipation channels exist that may lead to irreversible morphology changes. Therefore, for intense excitation of nanoparticles, e.g., in local thermolysis or particle modification such as fragmentation, excitation at the interband would be more efficient than excitation at the plasmon resonance wavelength. Yet, the proposed dark channels may add forces to particle modification that are not explored fully.

METHODS

Nanosol Synthesis. Gold colloids have been prepared by a physical method (PLAL) and chemical reactions. In PLAL, a solid gold target immersed in water was irradiated by 10 ps laser pulses of a Nd:YAG laser at 1064 nm.[17,65] The obtained multimodal size distribution is narrowed by centrifugation, redispersion and ripening steps to obtain two fractions with diameters of 23 and 53 nm (see Supporting Information) at a mass concentration of about 150 mg/L. The stability of the suspension is enhanced by adding electrolytes to form a 0.3 + 0.3 mM solution of NaCl and NaOH. Chemical synthesis has been performed by the citrate reduction (Turkevich method) at 100 °C, where size definition with a relatively narrow distribution of 12- 15% is achieved by a variable ratio of sodium tris(citrate) to

gold hydrochlorate.[66,67] As the final sizes form after an aggregation step the nanoparticles pertain a polycrystalline morphology.[68] Seeded synthesis, on the other hand,[28,69] allows for a better size definition and large crystal sizes, potentially leading to single crystalline particles. We have followed the recipe by Zheng et al.,[70] except for using cetyltrimethylammonium bromide (CTAB, Acros chemicals) only. In brief, gold seeds were prepared by the rapid reduction of gold hydrochloride by $NaBH_4$ in the presence of 100 mM of CTAB at 30 °C and rapid stirring. Seeded synthesis in several steps, depending on the final particle size, was performed in a stirred solution of 70 mM CTAB, 0.3 mM gold hydrochlorate, 5 mM ascorbic acid and a selected amount of seed by adding the seeds rapidly (first step) or continuously adding the growth solution over 2 h to a diluted seed suspension. The final suspension is either centrifuged (particles >30 nm) or decanted after CTAB crystallization at 6 °C to reduce the CTAB to a concentration of about 3 mM. The final mass concentration is set to about 50 mg/L. Size dispersion can be as low as 8%, but for the larger particles nonspherical shapes are observed, such as cubes or tetrahedra.

Particle sizes were determined by UV−vis spectroscopy, transmission electron microscopy (TEM, Zeiss EM 910, 80 kV) and X-ray small angle scattering (SAXS, synchrotron light source KARA). The determined sizes sizes vary in particular, if the size distribution is not Gaussian and because the relative weight of different sizes scales differently in TEM and SAXS. The SAXS sizes were used for discussing the size-dependent effects. We believe that this does not change the assertions in the following, as we analyze and discuss a large spectra of sizes with low size increment of the observables.

Sample Jet System. A liquid jet is driven by a syringe pump and formed at the orifice of an open glass capillary (Hilgenberg) of nominally 0.3 mm diameter in order to excite any portion of the sample only once. At the capillary exit a free round jet forms with a flow speed of 2.7 mL/min and a diameter of 0.26 mm at the beam intersection point. After excitation, the liquid is discarded. The laser beam is focused inside the round jet, such that the fluence varies with depth into the jet. Numerical simulations suggest that the total fluence change on the axis of the intersecting X-ray beam (which is much smaller than the jet diameter) amounts for about 20%, by partly balancing the increase by focusing with decrease by extinction with depth. Note that over a larger jet cross section this focusing can amount for up to 100%.[71]

Pump−Probe Setup. The jet is intersected by the pulsed X-ray beam along its diameter, the scattering of which is recorded on a charge-couple device (CCD) camera (Rayonix MX170-HS). The beam consists of pulses of 60 ps length (full width at half-maximum, fwhm) at a repetition rate of 1 kHz, as selected by a rotative chopper.[72] At the same time, time-synchronized laser pulses at 400 and 532 nm from a regenerative femtosecond amplifier (Coherent Legend) followed a frequency doubling in a nonlinear crystal or an optical parametric amplifier (Light Conversion,TOPAS), respectively, irradiate the same spot on the jet at a slight angle of 8 deg. The laser beam width is larger than the X-ray width (0.22 versus 0.02 mm fwhm). The time delay between both pulse trains can be varied with picosecond precision over the full interpulse spacing.

Calibration and Analysis Procedures. The laser beam profile on the sample has been modeled to derive a precise fluence value (see Figure S1) by measuring the profile in two orthogonal directions by a knife-edge scan by a thermal power meter (Coherent). The fluence is derived by averaging the profile over the X-ray illuminated cross sectional area. A continuous tuning of the laser power is achieved by a motorized wave plate combined with a Glan Laser polarizer. For 532 nm, the laser polarization was not purely linear so that the reached minimum fluence was limited.

Scattering on the detector is collected as 2D images with rotational symmetry around the direct beam due to the disordered suspension. Images were collected at a fixed delay between laser and X-ray pulses for 10−20 s each, averaging over $(1-2) \times 10^4$ excitation cycles. After image corrections (dark images, X-ray polarization, and solid angle correction of detection efficiency per pixel), the scattering signal was integrated azimuthally to yield one-dimensional scattering curves I(q) using $q = 4\pi/\lambda \cdot \sin(2\Theta/2)$, with X-ray wavelength $\lambda = 0.826$ Å and full scattering angle 2Θ. The scattering bears information on large-scale changes in the small-angle region, changes of the liquid scattering and a signal from crystalline nanoparticles. Here, we concentrate on the scattering from the gold particles, which can be observed as narrow peaks at given q values. Mainly the (111) powder peak around 2.67 $Å^{-1}$ is analyzed. No significant differences are found for the (200) reflection. We derive the lattice parameter shift $\Delta a/a$ from the shift of the powder peak as well as the reduction of the peak intensity. The latter may be caused by lattice heating through the increasing phonon-induced disorder and is quantified by the Debye−Waller factor B: $I(T,q) = I(0,q) \cdot \exp(-Bq^2)$.[73] Further intensity reduction can occur, if the particles undergo (partial) melting or destruction of the long-range order (e.g., by fragmentation).

Fluence-Dependent Bleaching. has been measured by applying laser pulses of 10 ps length at 532 nm from a 28.6 kHz train of a picosecond laser (IS400-1-L, Edgewave Würselen, Germany) to the suspension at variable laser pulse energy. A top-hat profile was achieved by a 1.5 mm pinhole. The gold colloid of 53 nm PLAL particles at 8.5 mg/L was placed in a 2 mL cuvette under constant stirring. Intensity before and after the cuvette was averaged over several pulses by a photo diode or averaged over the pulse train by a thermal power meter and used to calculate the as the ratio between these values as negative decadic logarithm for absorbance. Fluence was determined in a similar way.

Reference Spectra and Calculations. The scattering and absorption cross section of gold particles in water are calculated by Mie theory as available in common software distributions.[29] The total extinction can be compared to the measured extinction of the colloid samples, as represented in Figure 1. After scaling the measured spectra to the theoretical extinction, the general agreement between calculation and measured spectra is very good (compare Figure 1c). It should be noted that the plasmon peak in the range of 520−540 nm is slightly shifted to the red for the seeded particles. This is due to the effect of a CTAB shell around the particles, which has a higher refractive index than water and is not accounted for in the calculation. The impact on cross section is minor. For the calculation of the absorbed energy in the light field of the laser pulses only the theoretical cross sections are used. Assuming that the absorbed laser light is fully converted into heat and neglecting dissipation the temperature rise of the particles can be predicted. The fluence has been varied over a large range, which would yield a linearly varying lattice expansion (as manifestation of temperature change) as a function of fluence. The slope of this variation will be derived and compared to the theoretical calculations. An efficiency can

be defined by dividing the measured slope at low fluence by the expected slope by the Mie calculation.

Heat dissipation from the nanoparticles to the water surrounding has been calculated by an analytical Laplace approach,[32,52,74] assuming that the spreading of heat inside the gold sphere is instantaneous (justified by the high thermal conductivity and slow electron−phonon coupling) and dissipation is limited by the resistance across the gold-water interface (Kapitza resistance R_K[75]) plus bulk thermal diffusivity in water. The differential equation can be solved analytically in the limit of short laser pulses relative to the dissipation time. Variables in the fitting of the experimental time-resolved lattice expansion curves are the maximum temperature of the particles and R_K. Particle diameter, resolution of the X-ray probe, and water diffusivity are fixed input parameters. More details can be found in.[52]

AUTHOR INFORMATION

Corresponding Authors

Anton Plech − *Institute for Photon Science and Synchrotron Radiation, Karlsruhe Institute of Technology, D-76344 Eggenstein-Leopoldshafen, Germany;* orcid.org/0000-0002-6290-9303; Email: anton.plech@kit.edu

Sven Reichenberger − *Department of Technical Chemistry I and Center for Nanointegration Duisburg-Essen, University of Duisburg-Essen, D-45141 Essen, Germany;* orcid.org/0000-0002-7166-9428; Email: reichenberger@uni-due.de

Authors

Anna R. Ziefuß − *Department of Technical Chemistry I and Center for Nanointegration Duisburg-Essen, University of Duisburg-Essen, D-45141 Essen, Germany*

Matteo Levantino − *European Synchrotron Radiation Facility, F-38043 Grenoble, France;* orcid.org/0000-0002-1224-4809

René Streubel − *Department of Technical Chemistry I and Center for Nanointegration Duisburg-Essen, University of Duisburg-Essen, D-45141 Essen, Germany*

Stefan Reich − *Institute for Photon Science and Synchrotron Radiation, Karlsruhe Institute of Technology, D-76344 Eggenstein-Leopoldshafen, Germany;* Present Address: Fraunhofer Institute for High-Speed Dynamics, Ernst-Mach-Institute, Ernst-Zermelo-Straße 4, D-79104 Freiburg, Germany; orcid.org/0000-0002-8405-6540

Author Contributions

The research has been designed by A.R.Z., Sv.R. and A.P. The experiments have been performed by A.R.Z., Sv.R., M.L., St.R. and A.P. Analysis has been performed by A.R.Z., Sv.R. and A.P. The manuscript has been written by A.R.Z., Sv.R., and A.P. with input from all authors.

Funding

This work is supported by Deutsche Forschungsgemeinschaft under Project No.: 491072288 (PL325/10-1 and RE4672/2-1) and through research within "From Matter to Materials and Life" of the Helmholtz Association.

Notes

The authors declare no competing financial interest.

ACKNOWLEDGMENTS

We would like to acknowledge provision of beam time at ESRF (ID9) and KARA. Technical support by G. Buth is gratefully acknowledged. HR-TEM by H. Störmer, at the Laboratory for Electron Microscopy (LEM, KIT) is acknowledged. We enjoyed helpful discussions with L. Zhighilei.

REFERENCES

(1) Efros, A.; Nesbitt, D. Origin and control of blinking in quantum dots. *Nat. Nanotechnol.* **2016**, *11*, 661−671.

(2) Hirsch, L. R.; Stafford, R. J.; Bankson, J. A.; Sershen, S. R.; Rivera, B.; Price, R. E.; Hazle, J. D.; Halas, N. J.; West, J. L. Nanoshell-mediated near-infrared thermal therapy of tumors under magnetic resonance guidance. *Proc. Natl. Acad. Sci. U. S. A.* **2003**, *100*, 13549−13554.

(3) Abadeer, N. S.; Murphy, C. J. Recent Progress in Cancer Thermal Therapy Using Gold Nanoparticles. *J. Phys. Chem. C* **2016**, *120*, 4691−4716.

(4) Tatsuno, I.; Niimi, Y.; Tomita, M.; Terashima, H.; Hasegawa, T.; Matsumoto, T. Mechanism of transient photothermal inactivation of bacteria using a wavelength-tunable nanosecond pulsed laser. *Sci. Rep.* **2021**, *11*, 22310.

(5) Yao, C.; Rahmanzadeh, R.; Endl, E.; Zhang, Z.; Gerdes, J.; Hüttmann, G. Elevation of plasma membrane permeability by laser irradiation of selectively bound nanoparticles. *J. Biomed. Opt.* **2005**, *10*, 064012.

(6) Nan, N.; Si, D.; Hu, G. Nanoscale cavitation in perforation of cellular membraneby shock-wave induced nanobubble collapse. *J. Chem. Phys.* **2018**, *149*, 074902.

(7) Plech, A.; Boneberg, J.; Leiderer, P. Laser near-field ablation. *Laser & Phot. Rev.* **2009**, *3*, 435.

(8) Hashimoto, S.; Werner, D.; Uwada, T. Studies on the interaction of pulsed lasers with plasmonic gold nanoparticles toward light manipulation, heat management, and nanofabrication. *J. Photochem. Photobiol. C* **2012**, *13*, 28−54.

(9) Leiderer, P.; Bartels, C.; König-Birk, J.; Mosbacher, M.; Boneberg, J. Imaging optical near-fields of nanostructures. *Appl. Phys. Lett.* **2004**, *85*, 5370.

(10) Lukianova-Hleb, E. Y.; Hanna, E. Y.; Hafner, J. H.; Lapotko, D. O. Tunable plasmonic nanobubbles for cell theranostics. *Nanotechnology* **2010**, *21*, 085102.

(11) Ye, H.; Liu, Y.; Zhan, L.; Liu, Y.; Qin, Z. Signal amplification and quantification on lateral flow assays by laser excitation of plasmonic nanomaterials. *Theranostics* **2020**, *10*, 4359−4373.

(12) Huang, H.; Zhigilei, L. V. Atomistic view of laser fragmentation of gold nanoparticles in a liquid environment. *J. Phys. Chem. C* **2021**, *125*, 13413−13432.

(13) Li, W.; Chen, X. Gold nanoparticles for photoacoustic imaging. *Nanomedicine* **2015**, *10*, 299−320.

(14) Kumar, D.; Soni, R. K.; Ghai, D. P. Pulsed photoacoustic and photothermal response of gold nanoparticles. *Nanotechnology* **2020**, *31*, 035704.

(15) Qin, Z.; Wang, Y.; Randrianalisoa, J.; Raeesi, V.; Chan, W. C. W.; Lipiński, W.; Bischof, J. C. Quantitative Comparison ofPhotothermal Heat Generation between Gold Nanospheres and Nanorods. *Sci. Rep.* **2016**, *6*, 29836.

(16) Plech, A.; Ibrahimkutty, S.; Reich, S.; Newby, G. Thermal dynamics of pulsed-laser excited gold nanorods in suspension. *Nanoscale* **2017**, *9*, 17284−17292.
(17) Ziefuss, A. R.; Reich, S.; Reichenberger, S.; Levantino, M.; Plech, A. In situ structural kinetics of picosecond laser-induced heating and fragmentation of colloidal gold spheres. *Phys. Chem. Chem. Phys.* **2020**, *22*, 4993−5001.
(18) Kang, P.; Wang, Y.; Wilson, B.; Randrianalisoa, J.; Qin, Z.; et al. Nanoparticle fragmentation at solid state under single picosecond laser pulse stimulation. *J. Phys. Chem. C* **2021**, *125*, 26718−26730.
(19) Mo, M. Z.; et al. Heterogeneous to homogeneous melting transition visualized with ultrafast electron diffraction. *Science* **2018**, *360*, 1451−1455.
(20) Priyadarshini, M.; Adnan, M.; Prakash, G. V. Linear and nonlinear excitation induced ultrafast absorption dynamics in laser ablated and chemically synthesized gold nanoparticle colloids. *Opt. Mater.* **2021**, *117*, 111206.
(21) Geldhauser, T.; Kolloch, A.; Murazawa, N.; Ueno, K.; Boneberg, J.; Leiderer, P.; Scheer, E.; Misawa, H. Quantitative Measurement of the Near-Field Enhancement of Nanostructures by Two-Photon Polymerization. *Langmuir* **2012**, *28*, 9041−9046.
(22) Werner, D.; Hashimoto, S.; Uwada, T. Remarkable Photothermal Effect of Interband Excitation on Nanosecond Laser-Induced Reshaping and Size Reduction of Pseudospherical Gold Nanoparticles in Aqueous Solution. *Langmuir* **2010**, *26*, 9956−9963.
(23) Magnozzi, M.; Proietti Zaccaria, R.; Catone, D.; O'Keeffe, P.; Paladini, A.; Toschi, F.; Alabastri, A.; Canepa, M.; Bisio, F. Interband Transitions Are More Efficient Than Plasmonic Excitation in the Ultrafast Melting of Electromagnetically Coupled Au Nanoparticles. *J. Phys. Chem. C* **2019**, *123*, 16943−16950.
(24) Minutella, E.; Schulz, F.; Lange, H. Excitation-Dependence of Plasmon-Induced Hot Electrons in Gold Nanoparticles. *J. Phys. Chem. Lett.* **2017**, *8*, 4925−4929.
(25) Staechelin, Y. U.; Hoeing, D.; Schulz, F.; Lange, H. Size-Dependent Electron-Phonon Coupling in Monocrystalline Gold Nanoparticles. *ACS Photonics* **2021**, *8*, 752−757.
(26) Zhang, D.; Gökce, B.; Barcikowski, S. Laser Synthesis and Processing of Colloids: Fundamentals and Applications. *Chem. Rev.* **2017**, *117*, 3990−4103.
(27) Turkevich, J.; Stevenson, P. C.; Hillier, J. A Study of the Nucleation and Growth Processes in the Synthesis of Colloidal Gold. *Discuss. Faraday Soc.* **1951**, *11*, 55.
(28) Jana, N. R.; Gearheart, L.; Murphy, C. J. Seed-Mediated Growth Approach for Shape-Controlled Synthesis of Spheroidal and Rod-Like Gold Nanoparticles Using a Surfactant Template. *Adv. Mater.* **2001**, *13*, 1389−1393.
(29) Laven, P. Simulation of rainbows, coronas, and glories by use of Mie theory. *Appl. Opt.* **2003**, *42*, 436−444.
(30) Shih, C.-Y.; Streubel, R.; Heberle, J.; Letzel, A.; Shugaev, M. V.; Wu, C.; Schmidt, M.; Gökce, B.; Barcikowski, S.; Zhigilei, L. V. Two mechanisms of nanoparticle generation in picosecond laser ablation in liquids: the origin of the bimodal size distribution. *Nanoscale* **2018**, *10*, 6900−6910.
(31) Reich, S.; Letzel, A.; Menzel, A.; Kretzschmar, N.; Gökce, B.; Barcikowski, S.; Plech, A. Early appearance of crystalline nanoparticles in pulsed laser ablation in liquids dynamics. *Nanoscale* **2019**, *11*, 6962−6969.
(32) Plech, A.; Kotaidis, V.; Grésillon, S.; Dahmen, C.; von Plessen, G. Laser-Induced heating and melting of gold nanoparticles studied by time-resolved x-ray scattering. *Phys. Rev. B* **2004**, *70*, 195423.
(33) Plech, A.; Krause, B.; Baumbach, T.; Zakharova, M.; Eon, S.; Bracht, H.; et al. Structural and thermal characterisation of nanolayers by time-resolved X-ray scattering. *nanomaterials* **2019**, *9*, 501.
(34) Kotaidis, V.; Dahmen, C.; von Plessen, G.; Springer, F.; Plech, A. Excitation of nanoscale vapor bubbles at the surface of gold nanoparticles in water. *J. Chem. Phys.* **2006**, *124*, 184702.
(35) Diroll, B. T.; Brumberg, A.; Leonard, A. A.; Panuganti, S.; Watkins, N. E.; Cuthriell, S. A.; Harvey, S. M.; Kinigstein, E. D.; Yu, J.; Zhang, X.; Kanatzidis, M. G.; Wasielewski, M. R.; Chen, L. X.; Schaller, R. D. Photothermal behaviour of titanium nitride nanoparticles evaluated by transient X-ray diffraction. *Nanoscale* **2021**, *13*, 2658−2664.
(36) Hartland, G. V. Measurements of the material properties of metal nanoparticles by time-resolved spectroscopy. *Phys. Chem. Chem. Phys.* **2004**, *6*, 5263−5274.
(37) van Dijk, M. A.; Lippitz, M.; Orrit, M. Detection of Acoustic Oscillations of Single Gold Nanospheres by Time-Resolved Interferometry. *Phys. Rev. Lett.* **2005**, *95*, 267406.
(38) Kotaidis, V.; Dekorsy, T.; Ibrahimkutty, S.; Issenmann, D.; Khakhulin, D.; Plech, A. Vibrational symmetry breaking of supported nanospheres. *Phys. Rev. B* **2012**, *86*, 100101.
(39) Plech, A.; Grésillon, S.; von Plessen, G.; Scheidt, K.; Naylor, G. Structural kinetics of laser-excited metal nanoparticles supported on a surface. *Chem. Phys.* **2004**, *299*, 183.
(40) Plech, A.; Kotaidis, V.; Lorenc, M.; Boneberg, J. Femtosecond laser near-field ablation from gold nanoparticles. *Nat. Phys.* **2006**, *2*, 44−47.
(41) Takami, A.; Kurita, H.; Koda, S. Laser-Induced Size Reduction of Noble Metal Particles. *J. of Phys. Chem. B* **1999**, *103*, 1226−1232.
(42) Touloukian, Y. S.; Kirby, R. K.; Taylor, R. E.; Desai, P. D. *Thermal expansion - Metallic elements and alloys*; Thermodynamical Properties of Matter 12; IFI Plenum: New York, 1975.
(43) Ahmadi, T. S.; Logunov, S. L.; El-Sayed, M. A. Picosecond dynamics of colloidal gold nanoparticles. *J. Phys. Chem.* **1996**, *100*, 8053−8056.
(44) Lin, Z.; Zhigilei, L. V.; Celli, V. Electron-phonon coupling and electron heat capacity of metals under conditions of strong electron phonon nonequilibrium. *Phys. Rev. B* **2008**, *77*, 075133.
(45) Sygletou, M.; Benedetti, S.; Ferrera, M.; Pierantozzi, G. M.; Cucini, R.; Della Valle, G.; Carrara, P.; De Vita, A.; di Bona, A.; Torelli, P.; Catone, D.; Panaccione, G.; Canepa, M.; Bisio, F. Quantitative Ultrafast Electron-Temperature Dynamics in Photo-Excited Au Nanoparticles. *Small* **2021**, *17*, 2100050.
(46) Rudnitzki, F.; Bever, M.; Rahmanzadeh, R.; Brieger, K.; Endl, E.; Groll, J.; Hüttmann, G. Bleaching of plasmon-resonance absorption of gold nanorods decreases efficiency of cell destruction. *J. Biomed. Opt.* **2012**, *17*, 058003.
(47) Zhang, X.; Huang, C.; Wang, M.; Huang, P.; He, X.; Wei, Z. Transient localized surface plasmon induced by femtosecond interband excitation in gold nanoparticles. *Sci. Rep.* **2018**, *8*, 10499.
(48) Link, S.; El-Sayed, M. A. *Int. Reviews in Phys. Chem.* **2000**, *19*, 409−453.
(49) Lin, Z.; Zhigilei, L. V. Thermal excitation of d band electrons in Au: implications for laser-induced phase transformations. *Proc. SPIE* **2006**, *6261*, 62610U.
(50) Aruda, K. O.; Tagliazucchi, M.; Sweeney, C.; Hannah, D. C.; Schatz, G. C.; Weiss, E. A. Identification of parameters through which surface chemistry determines the lifetimes of hot electrons in small Au nanoparticles. *Proc. Natl. Acad. Sci. U.S.A.* **2013**, *110*, 4212−4217.
(51) Neumann, J.; Brinkmann, R. Self-limited growth of laser-induced vapor bubbles around single microabsorbers. *Appl. Phys. Lett.* **2008**, *93*, 033901.
(52) Siems, A.; Weber, S. A. L.; Boneberg, J.; Plech, A. Thermodynamics of nanosecond nanobubble formation at laser-excited metal nanoparticles. *New. J. Phys.* **2011**, *13*, 043018.
(53) Kotaidis, V.; Plech, A. Cavitation dynamics on the nanoscale. *Appl. Phys. Lett.* **2005**, *87*, 213102.
(54) Wang, L.; Rossi, T.; Oppermann, M.; Bauer, B.; Mewes, L.; Zare, D.; Chow, T. H.; Wang, J.; Chergui, M. Slow Charge Carrier Relaxation in Gold Nanoparticles. *J. Phys. Chem. C* **2020**, *124*, 24322−24330.
(55) Hwang, Y.-N.; Jeong, D. H.; Shin, H. J.; Kim, D.; Jeoung, S. C.; Han, S. H.; Lee, J.-S.; Cho, G. Femtosecond Emission Studies on Gold Nanoparticles. *J. Phys. Chem. B* **2002**, *106*, 7581−7584.
(56) Dulkeith, E.; Niedereichholz, T.; Klar, T. A.; Feldmann, J.; von Plessen, G.; Gittins, D. I.; Mayya, K. S.; Caruso, F. Plasmon emission in photoexcited gold nanoparticles. *Phys. Rev. B* **2004**, *70*, 205424.
(57) Filipczak, P.; Pastorczak, M.; Kardas, T.; Nejbauer, M.; Radzewicz, C.; Kozanecki, M. Spontaneous versus Stimulated Sur-

face-Enhanced Raman Scattering of Liquid Water. *J. Phys. Chem. C* **2021**, *125*, 1999−2004.
(58) Yamada, K.; Tokumoto, Y.; Nagata, T.; Mafuné, F. Mechanism of Laser-induced Size-reduction of Gold Nanoparticles as Studied by Nanosecond Transient Absorption Spectroscopy. *J. Phys. Chem. B* **2006**, *110*, 11751−11756.
(59) Werner, D.; Furube, A.; Okamoto, T.; Hashimoto, S. Femtosecond Laser-Induced Size Reduction of Aqueous Gold Nanoparticles: In Situ and Pump-Probe Spectroscopy Investigations Revealing Coulomb Explosion. *J. Phys. Chem. C* **2011**, *115*, 8503−8512.
(60) Boulais, E.; Lachaine, R.; Meunier, M. Plasma-Mediated Nanocavitation and Photothermal Effects in Ultrafast Laser Irradiation of Gold Nanorods in Water. *J. Phys. Chem. C* **2013**, *117*, 9386−9396.
(61) Zhao, C.; An, W.; Zhang, Y.; Dong, Q.; Gao, N. A Molecular Dynamics Analysis on Interfacial Thermal Resistance between Particle and Medium in Light-Induced Heat Transfer of Plasmonic Nanofluid. *Langmuir* **2022**, *38*, 2327−2334.
(62) Graf, M.; Vonbun-Feldbauer, G. B.; Koper, M. T. M. Direct and Broadband Plasmonic Charge Transfer to Enhance Water Oxidation on a Gold Electrode. *ACS Nano* **2021**, *15*, 3188−3200.
(63) Simakin, A. V.; Astashev, M. E.; Baimler, I. V.; Uvarov, O. V.; Voronov, V. V.; Vedunova, M. V.; Sevost'yanov, M. A.; Belosludtsev, K. N.; Gudkov, S. V. The Effect of Gold Nanoparticle Concentration and Laser Fluence on the Laser-Induced Water Decomposition. *J. Phys. Chem. B* **2019**, *123*, 1869−1880.
(64) Minelli, C.; et al. (102 authors), Versailles project on advanced materials and standards (VAMAS) interlaboratory study on measuring the number concentration of colloidal gold nanoparticles. *Nanoscale* **2022**, *14*, 4690−4704.
(65) Ziefuß, A. R.; Reichenberger, S.; Rehbock, C.; Chakraborty, I.; Gharib, M.; Parak, W. J.; Barcikowski, S. Laser Fragmentation of Colloidal Gold Nanoparticles with High-Intensity Nanosecond Pulses is Driven by a Single-Step Fragmentation Mechanism with a Defined Educt Particle-Size Threshold. *J. Phys. Chem. C* **2018**, *122*, 22125−22136.
(66) Frens, G. Controlled Nucleation for the Regulation of the Particle Size in Monodisperse Gold Suspensions. *Nat. Phys. Sci.* **1973**, *241*, 20−22.
(67) Kimling, J.; Maier, M.; Okenve, B.; Kotaidis, V.; Ballot, H.; Plech, A. Turkevich Method for Gold Nanoparticle Synthesis Revisited. *J. Phys. Chem. B* **2006**, *110*, 15700.
(68) Plech, A.; Siems, A.; Kotaidis, V.; Sztucki, M. Kinetics of the X-ray Induced Gold Nanoparticle Synthesis. *Phys. Chem. Chem. Phys.* **2008**, *10*, 3888.
(69) Rodríguez-González, B.; Mulvaney, P.; Liz-Marzán, L. M. An Electrochemical Model for Gold Colloid Formation via Citrate Reduction. *Z. Phys. Chem.* **2007**, *221*, 415.
(70) Zheng, Y.; Zhong, X.; Li, Z.; Xia, Y. Successive, Seed-Mediated Growth for the Synthesis of Single-Crystal Gold Nanospheres with Uniform Diameters Controlled in the Range of 5−150 nm. *Part. Part. Syst. Charact.* **2014**, *31*, 266−273.
(71) Zerebecki, S.; Reichenberger, S.; Barcikowski, S. Continuous-Flow Flat Jet Setup for Uniform Pulsed Laser Postprocessing of Colloids. *J. Phys. Chem. A* **2020**, *124*, 11125−11132.
(72) Cammarata, M.; Eybert, L.; Ewald, F.; Reichenbach, W.; Wulff, M.; Anfinrud, P.; Schotte, F.; Plech, A.; Kong, Q.; Lorenc, M.; Lindenau, B.; Räbiger, J.; Polachowski, S. Optimized shutter train operation for high brightness synchrotron pump-probe experiment. *Rev. Sci. Instrum.* **2009**, *80*, 015101.
(73) Ziman, J. M. *Principles of the Theory of Solids*, 2nd ed.; Cambridge University Press: London, 1972.
(74) Chahine, G. L., Frederick, G. S., Lambrecht, C. J., Harris, G. S., Mair, H. U. Spark-generated bubbles as laboratory-scale models of underwater explosions and their use for validation of simulation tools*SAVIAC Proceedings of the 66th Shock and Vibrations Symposium: October 30 - November 3, 1995, Biloxi, MS*; Shock & Vibration Information Analysis Center: Arvonia, VA, 1995.
(75) Wilson, O. M.; Hu, X.; Cahill, D. G.; Braun, P. V. Colloidal metal particles as probes of nanoscale thermal transport in fluids. *Phys. Rev. B* **2002**, *66*, 224301.